

An Inactivation Gate of the BsYetJ Calcium Channel That Becomes Functional in the Endoplasmic Reticulum Environment

Yu-Jing Lan

National Tsing Hua University

Chu-Chun Cheng

National Tsing Hua University

Shu-Chi Chu

National Tsing Hua University

Hung-Ying Chen

National Tsing Hua University

Chieh-Chin Li

Weill Cornell Medicine

Te-Yu Kao

National Tsing Hua University <https://orcid.org/0000-0002-3286-3287>

Yun-Wei Chiang (✉ ywchiang@mx.nthu.edu.tw)

National Tsing Hua University <https://orcid.org/0000-0002-2101-8918>

Article

Keywords:

Posted Date: May 12th, 2022

DOI: <https://doi.org/10.21203/rs.3.rs-1567633/v1>

License:  This work is licensed under a Creative Commons Attribution 4.0 International License.

[Read Full License](#)

An Inactivation Gate of the BsYetJ Calcium Channel That Becomes Functional in the Endoplasmic Reticulum Environment

Yu-Jing Lan¹, Chu-Chun Cheng¹, Shu-Chi Chu¹, Hung-Ying Chen¹, Chieh-Chin Li^{1,2}, Te-Yu Kao¹, and Yun-Wei Chiang^{1*}

¹Department of Chemistry, National Tsing Hua University, Hsinchu 300-044, Taiwan

²Department of Physiology and Biophysics, Weill Cornell Medical College, New York, NY 10065, USA

*Corresponding email: ywchiang@mx.nthu.edu.tw

Abstract

The transmembrane BAX inhibitor-1-containing motif 6 (TMBIM6) is an anti-apoptotic endoplasmic reticulum (ER) membrane protein. The suppression of apoptosis by TMBIM6 is linked to its role in regulating calcium homeostasis. However, the molecular mechanisms underlying the calcium regulation in the ER remain poorly understood. Using mutagenesis and fluorescence-based functional assays, this study investigates all the highly conserved negatively charged residues in the BsYetJ (a bacterial homolog of TMBIM6) and reveals that the charged residues E49 and R205 cooperatively act as a calcium-selectivity filter determining the channel conductance. This study identifies the conformations of BsYetJ in the ER environment using electron spin resonance and molecular dynamics. Together with the functional data, these previously undescribed structures provide new insights of how BsYetJ regulates calcium-dependent inactivation by interconversion between two coexisting conformations. Overall, this study provides a framework for understanding the non-canonical calcium gated membrane protein, which will facilitate structure-based development of more effective medications for TMBIM6.

Introduction

The transmembrane BAX inhibitor-1-containing motif (TMBIM) family is widely conserved across species; it is present in prokaryotes, fungi, plants, and mammals^{1–6}. Humans, for example, have six identified TMBIM proteins (TMBIM 1 to 6), each containing seven presumed transmembrane (TM) helices with variations in sequence and length. However, none of the six members has been structurally determined. TMBIM6 is identified as a suppressor of programmed cell death. Recently, TMBIM6 has been reported to play an important role in the regulation of aging in mice and humans, and to be closely associated with survival in patients with cervical, breast, lung, and prostate cancers⁷. The structure-function relationship of TMBIM6, however, remains poorly understood.

Accumulating evidence has suggested a role of TMBIM6 in regulating calcium release^{3,7,8}. It showed that BsYetJ (*Bacillus subtilis* bacterial homolog of TMBIM6) functionally uptakes Ca²⁺ in *E. coli* and operates in a pH-dependent manner in proteoliposomes^{9–11}. Crystal studies revealed that BsYetJ (solubilized in detergent) adopts two distinct conformations at pH 7, with TM2 undergoing conformational changes⁹. Structurally, BsYetJ (a monomer consisting of 214 amino acids) is unlike canonical calcium channels displaying a well-defined oligomeric pore. When reconstituted into nanodiscs containing pure 1-palmitoyl-2-oleoyl-sn-glycero-3-phosphocholine (POPC) lipid and studied using the double electron-electron resonance (DEER) spectroscopy^{12–14}, BsYetJ was reported to adopt multiple conformations and exhibit a pH-dependent behavior different from what was found in detergent-solubilized states¹¹. These findings stimulate a model of calcium-release channel showing that the calcium channel functioning can be modulated through the interconversion between distinct conformations in the preexisting conformational equilibria of BsYetJ.

One important message from the previous studies is that the surrounding environment can significantly influence a membrane protein; that the structure of BsYetJ is different between detergent and pure POPC environments implies an important role of the surrounding environment in determining the functional and structural integrity of BsYetJ. It is thus urgently needed to take into consideration of lipid environment when studying structure-function relationship of BsYetJ. Several studies have reported that the composition of lipids is

critical for preserving the structural and functional properties of membrane proteins. For example, the conformation of the nicotinic acetylcholine receptor (nAChR) in POPC-only liposomes was found to be altered causing the loss of allosteric coupling between agonist-binding sites and TM pore¹⁵. Cheng et al. showed that the human inward-rectifying potassium channel Kir2.1 becomes functionally inactive in liposomes containing pure 1-Palmitoyl-2-oleoyl-sn-glycero-3-phosphoethanolamine (POPE) or POPC lipids¹⁶. ELIC, a pentameric ligand-gated ion channel, reconstituted in a POPC environment was found to frustrate the coupling between extracellular and transmembrane domains, and therefore fail to elicit its intrinsic ion-flux activity upon agonist binding^{17,18}. Therefore, it is critical that such investigations of membrane protein be carried out in a lipid bilayer reminiscent of their native environment.

TMBIM6 localizes to the endoplasmic reticulum (ER), where it inhibits apoptosis sensitive to ER-stress responses such as etoposide and staurosporine³. The suppression of apoptosis by TMBIM6 is directly or indirectly linked to its role in regulating Ca²⁺ homeostasis^{3,8,19}. However, the Ca²⁺ binding/gating sites of TMBIM6/BsYetJ have not been determined. To explore the calcium regulation mechanism, this study conducts a comprehensive investigation on the conformations of BsYetJ reconstituted in nanodiscs with a lipid environment mimicking the ER. We measure the calcium flux activity of various BsYetJ variants and carry out pulsed electron spin resonance (ESR) DEER technique to measure the distances between selected spin-label pairs in BsYetJ. The conformations of BsYetJ are revealed in apo state (metal ion-free) by using choline chloride as a substitute for metal ions¹¹, and in holo state (i.e., in the presence of Ca²⁺). Our results uncover the calcium-dependent inactivation of BsYetJ, a fundamental regulatory mechanism that has not been reported for BsYetJ.

RESULTS

There are totally ten negatively charged residues in BsYetJ: E7 (TM1), E49 (TM2), E99 (TM4), D121 (TM5), D171 (TM6), E182 (TM7), D183 (TM7), D195 (TM7), D213 (TM7), and D214 (TM7), where six of them are identified as highly conserved and important residues (Figs. 1A and S1A). It remains unclear as to what roles these highly conserved

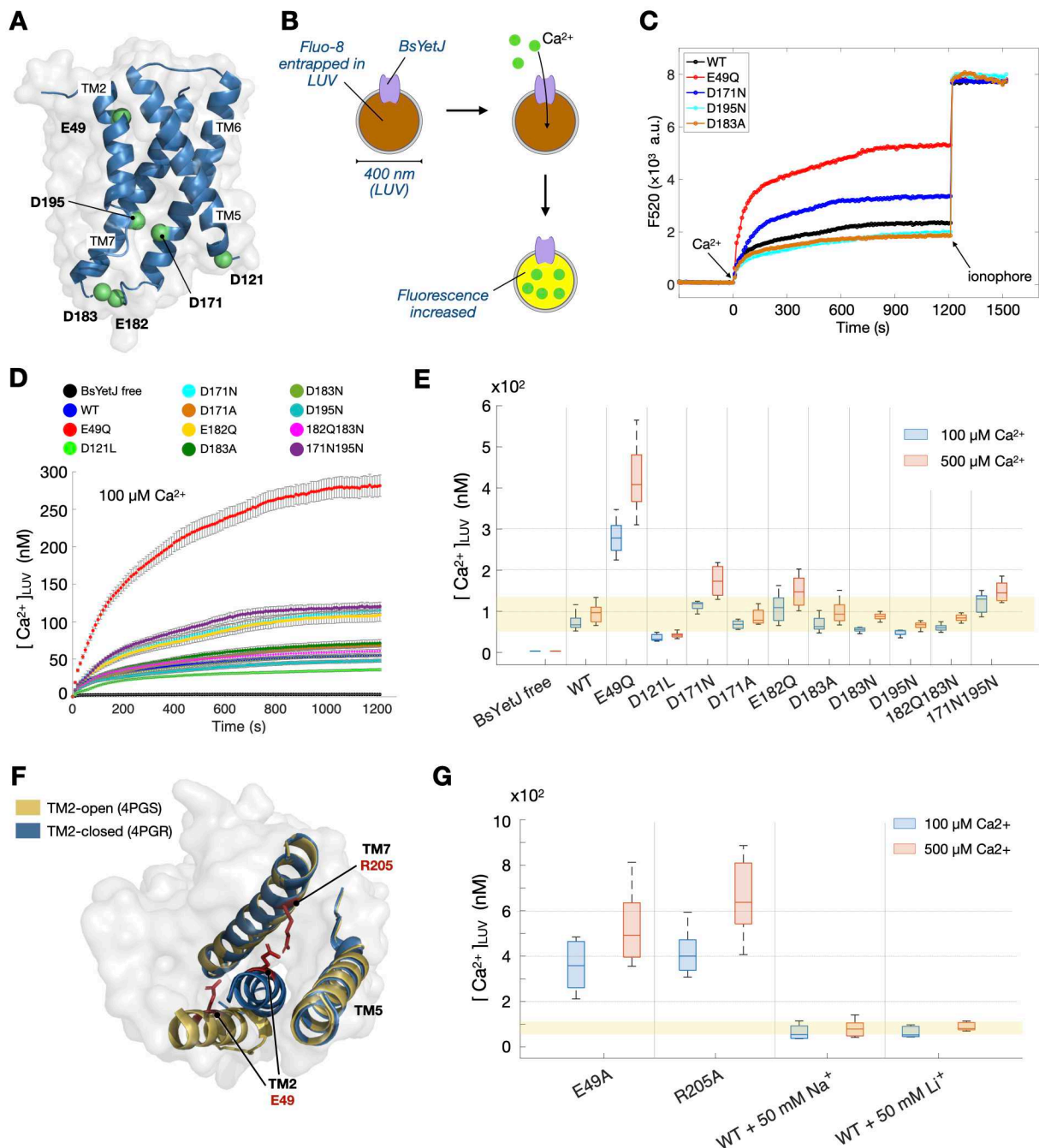


Fig. 1. Measurements of Ca²⁺ influx activity. (A) Positions of the six highly conserved negatively charged residues. (B) Illustration for the measurement of Ca²⁺ influx activity of BsYetJ. (C) Some representative data of the time-dependent changes in F520 intensity (100 μM ∇Ca²⁺). (D) Results for the [Ca²⁺]_{LUV} (100 μM ∇Ca²⁺), calculated from the F520 data. Data are shown as mean ± SDE ($n = 10$). (E) Data of final [Ca²⁺]_{LUV} for the BsYetJ variants studied. (F) Crystal structures showing E49 and R205 are spatially closed. (G) Data of final [Ca²⁺]_{LUV} for BsYetJ E49A and R205A. Also, [Ca²⁺]_{LUV} data for WT measured after the external addition of 50 mM Na⁺ or Li⁺. All [Ca²⁺]_{LUV} data shown are presented by the box-and-whisker diagram showing the median, the lower and upper quartiles, and the minimum and maximum values. Yellow stripe in E and G covers the extrema of WT data.

residues play in the regulation of Ca^{2+} transport activity of BsYetJ. To address their individual roles, we reconstituted BsYetJ variants into large unilamellar vesicles (LUV) composed of the lipid composition of ER membranes and then performed the calcium influx measurements (Fig. 1B) at pH 7.4. Basically, the Ca^{2+} transport activity of BsYetJ is evaluated by measuring changes in the fluorescence intensity of Fluo-8 (Fig. S1B) at 520 nm (hereafter, denoted by F520), which reflects the fraction of the entrapped Fluo-8 that forms a complex with the transported Ca^{2+} from the outside of LUVs inwards, within a fixed duration of time (see Methods for details).

Measurements of Ca^{2+} transport activity of BsYetJ variants

This study measured the time-dependent F520 fluorescence intensity after adding calcium to have a concentration of 100 μM Ca^{2+} in the solution containing calcium-free BsYetJ/LUV proteoliposomes (Fig. 1C). Upon the addition of calcium, which establishes a calcium electrochemical gradient (∇Ca^{2+}) across the membrane bilayer of LUV, we observed that F520 intensity increases with time, depending on the BsYetJ variants reconstituted. Most of samples studied reached to a steady state in F520 within 900 s after the addition of calcium. At time around 1200 s, calcium ionophore (ionomycin), which can efficiently transport Ca^{2+} across LUV membranes, was added into the medium to obtain the F520 intensity for the saturation condition ($\nabla\text{Ca}^{2+} \sim 0$). The F520 data were analyzed to yield the accumulated concentration of Ca^{2+} within the LUVs (denoted by $[\text{Ca}^{2+}]_{\text{LUV}}$, hereafter) over the 1200 s incubation time. A representative result is shown (Fig. 1D) displaying how $[\text{Ca}^{2+}]_{\text{LUV}}$ changes with time after ∇Ca^{2+} (100 μM) is established and how it depends on BsYetJ variants. This study has performed two different ∇Ca^{2+} (100 and 500 μM ; see also Fig. S1C) and repeated the measurements of each BsYetJ variant as well as BsYetJ-free LUVs (as a control), for at least ten times each. The recorded $[\text{Ca}^{2+}]_{\text{LUV}}$ (Fig. 1E) reflects the measures of Ca^{2+} transport activity of BsYetJ as it increases with ∇Ca^{2+} . In the measurements with BsYetJ-free LUVs, the addition of calcium (100 or 500 μM) induces no calcium permeability in LUVs.

E49 regulates the Ca^{2+} transport activity of BsYetJ

We observed that in either of the ∇Ca^{2+} values (100 or 500 μM), wild-type (WT) BsYetJ allows some calcium influx until $[\text{Ca}^{2+}]_{\text{LUV}}$ reaches around 100 nM, which is much lower than the calcium concentration outside the LUVs and the concentration of entrapped Fluo-8 (10 μM). It suggests that the presence of ∇Ca^{2+} promotes the calcium influx activity, but there is a gating mechanism in BsYetJ that works against the calcium influx from a higher Ca^{2+} concentration. The similar gating behavior can be observed in all the BsYetJ variants studied (Fig. 1E). Variants D121L, D171A, D183A, D183N, D195N, E182Q/D183N have $[\text{Ca}^{2+}]_{\text{LUV}}$ values moderately close to those of WT (indicated by a yellow stripe in Fig. 1E). The rest of BsYetJ variants have $[\text{Ca}^{2+}]_{\text{LUV}}$ values greater than those measured for WT. Particularly, E49Q exhibits a much greater value of $[\text{Ca}^{2+}]_{\text{LUV}}$ than others, suggesting that the mutation E49Q causes a large disruption to the gating mechanism and thus allows a large amount of Ca^{2+} influx increasing $[\text{Ca}^{2+}]_{\text{LUV}}$ to be 4-5 times greater than that of WT.

Previous studies indicate that BsYetJ at pH 7 adopts at least two distinct conformations, which are hereafter referred to as TM2-open and TM2-closed as the major difference occurs in TM2 (Fig. 1F)^{9,11}. An inspection of the TM2-closed model indicates that the residues E49 and R205 are spatially close to each other (Fig. 1F), but their importance has not been investigated. To verify the importance of the two residues, we performed the Fluo-8 assay on two more BsYetJ variants carrying single mutations, E49A and R205A. The $[\text{Ca}^{2+}]_{\text{LUV}}$ values obtained (Fig. 1G) are as high as, or higher than those of E49Q.

Besides, we performed the Ca^{2+} influx assay in the presence of Ca^{2+} and other ions. The $[\text{Ca}^{2+}]_{\text{LUV}}$ results for WT (Fig. 1G) are basically not affected by the presence of other ions (Na^+ or Li^+), supporting the selectivity of BsYetJ for Ca^{2+} . The selectivity found here is different from an earlier report¹⁰ that affinity of detergent-solubilized BsYetJ for Ca^{2+} is largely inhibited by the presence of Na^+ or Li^+ . Collectively, our results indicate that the E49-R205 dyad forms a calcium-selectivity filter determining the Ca^{2+} influx activity of BsYetJ in the ER environment.

BsYetJ conformations in the ER nanodiscs

To explore what differences in the conformations of BsYetJ in the ER versus BsYetJ crystals and identify the changes between apo and holo (20 mM Ca^{2+}) states, we performed DEER

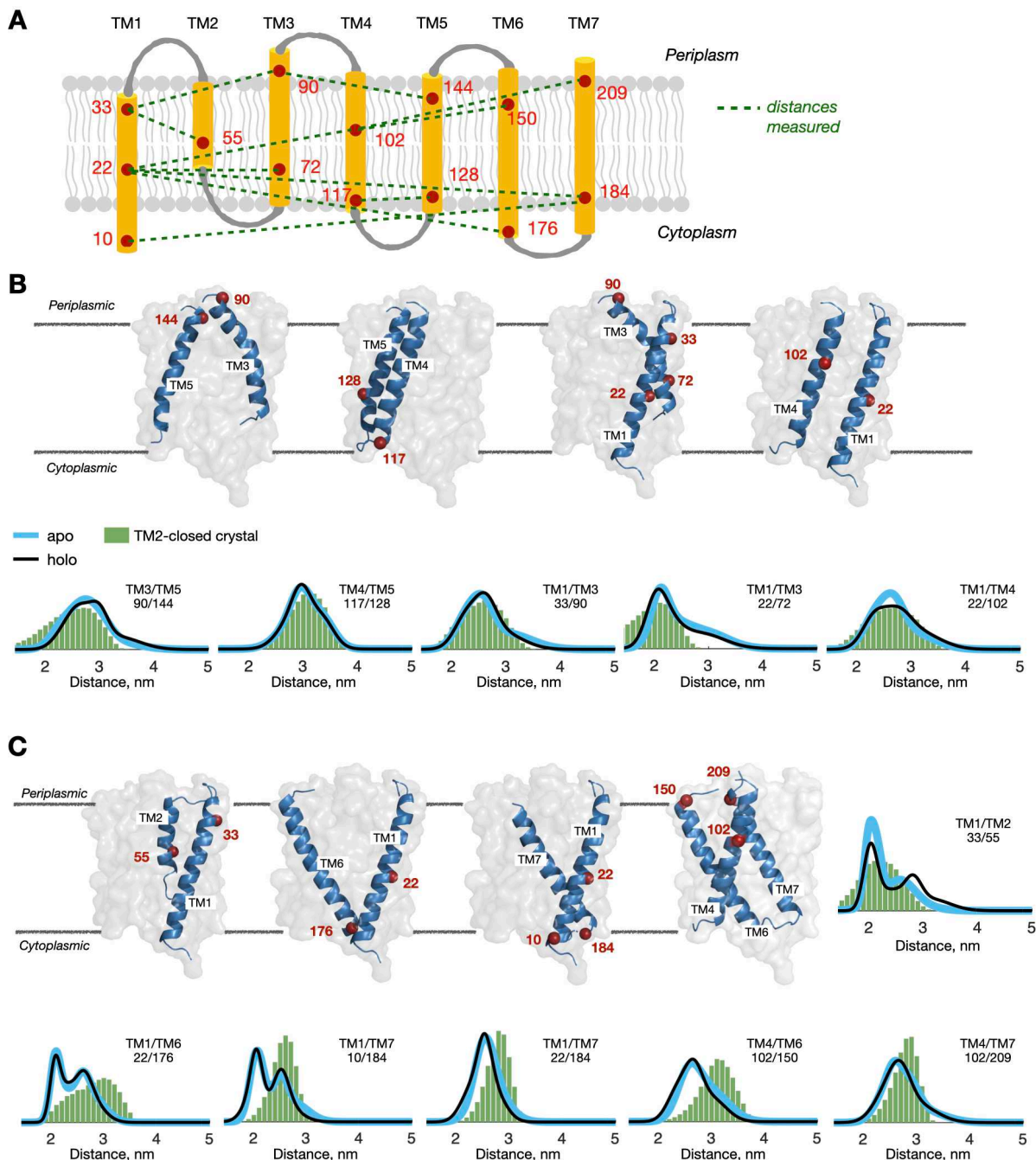


Fig. 2. Results of the DEER measurements for apo and holo BsYetJ. (A) Topology of a BsYetJ with spin-labeled sites shown as red spheres. Green dashed lines indicate the measured distances. (B) Distance distributions that show little change between apo and holo states. The conformations of TM1, TM3, TM4, and TM5 resemble the TM2-closed crystal structure (4PGR). (C) Distance distributions of BsYetJ in the ER nanodiscs that display differences from the TM2-closed crystal. The results of 33/55 exhibit the most prominent changes between apo and holo states among all distance distributions measured.

measurements on various double-labeled BsYetJ (Fig. 2A) embedded in the ER lipid nanodiscs (pH 7.4), one at a time, and then extracted the interspin distance distributions from

the experimental DEER data (see Fig. S2 for raw DEER traces) using the Tikhonov-based regulation methods^{20,21}. We first show (Fig. 2B) the results of distance distributions corresponding to the inter-helical distances between TM1, TM3, TM4, and TM5. As the distance distributions are similar between apo and holo states, the results indicate that the four TM helices in the ER nanodiscs are basically unchanged in the presence and absence of calcium. Also, their inter-helical distances are reasonably consistent with the TM2-closed crystal (pale green histograms in Fig. 2B; PDB: 4PGR). These TM helices can thus be taken as a reference for identifying conformational changes of other TM helices between apo and holo states, as demonstrated in the following.

Using helices TM1 and TM4 as a reference, we measured distances of TM2, TM6, and TM7 relative to individual reference helices (Fig. 2C). The distance distributions of 33/55, which correspond to the cytoplasmic side of TM2 in BsYetJ, exhibit the largest difference between apo and holo states, among all distance distributions obtained herein. While the component of shorter distances remained unchanged at 2 nm in response to the presence of calcium, the component of longer distances increased evidently from 2.6 nm (apo) to 2.8 nm (holo), accompanying with a change in the corresponding population from 49% to 61% (estimated from the area of distance distributions). We also observed bimodal-like distance distributions when a spin label is attached to the cytoplasmic side of TM6 or TM7 (see 22/176 and 10/184 in Fig. 2C). When a spin label is attached to the periplasmic side of TM6 or TM7 (see 102/150 and 102/209 in Fig. 2C), the distance distributions appear to be more homogeneous.

Collectively, our results show that TM2 is the most sensitive to calcium. As opposed to the TM2-closed crystal structure, the conformations of TM2, TM6 and TM7 in the ER are somewhat altered. In a comparison of BsYetJ in the ER nanodiscs and the previously reported BsYetJ in pure POPC nanodiscs (Fig. S3), the most striking difference is that TM2 in pure POPC nanodiscs changes insignificantly between apo and holo. Indeed, lipid environment plays an important role in determining the BsYetJ conformations.

BsYetJ E49Q conformations

Next, we performed DEER measurements on double-labeled BsYetJ E49Q variants in the ER nanodiscs, in apo and holo states, to obtain the structure-based evidence for how E49Q causes a large change to the Ca^{2+} influx activity. The results (Fig. 3A) show that the distance distributions are generally consistent between BsYetJ with versus without E49Q, with a few exceptions detailed below. With E49Q, the bimodal-like distance distributions of 10/184 and 22/176 appear to shift toward the population of longer distances, with a feature of becoming broader and less heterogeneity. A similar observation can be obtained from 90/144 E49Q, though the distance distributions shift to shorter distances. The most noteworthy aspect of the E49Q results is that the DEER traces of 33/55 and 33/90 suffer from lack of clear dipolar modulation depths (Fig. 3B), representing the largest reduction in the modulation depth (ΔV_m) of E49Q data as compared with the DEER traces without E49Q. Due to the lack of ΔV_m , which leads to very low SNR (signal-to-noise ratio), the recovered distance distributions of 33/55 and 33/90 for E49Q thus contain substantial uncertainty and are not displayed. The significant reduction in ΔV_m suggests that the mutation E49Q brings about a disruption in the interactions of E49 and R205 (Fig. 3C) and thus the N terminal of TM2, which subsequently renders TM2 into a dangling conformation. As a result, the segment connecting TM2 and TM1 (where site 33 is located; Fig. 3C) of BsYetJ E49Q resides in a highly disordered state, causing a reduction in ΔV_m . An overview of all DEER traces is provided (Fig. S2) showing also that as opposed to the result of 33/90 E49Q, the DEER traces of 90/144 E49Q are characterized by distinct ΔV_m in both apo and holo states. In view of these observations, we concluded that the increased disordering in 33/55 E49Q is mainly caused by the change in the local environment of site 33.

To support the above conclusion, this study collected CW-ESR spectra of 33/55 with and without E49Q at 300 K (Fig. 3D). The spectrum of 33/55 with E49Q apparently consists of a component with a sharper feature, which reflects a greater mobility in the local environment, than the spectrum without E49Q. As the measurements were performed above room temperatures and the interspin distances of 33/55 are sufficiently large (>2 nm) to avoid the dipolar broadening, the spectral differences reflect changes in nitroxide mobility primarily associated with the local environment of site 33. It demonstrates that the local dynamics and disordering of 33/55 are clearly increased in BsYetJ E49Q.

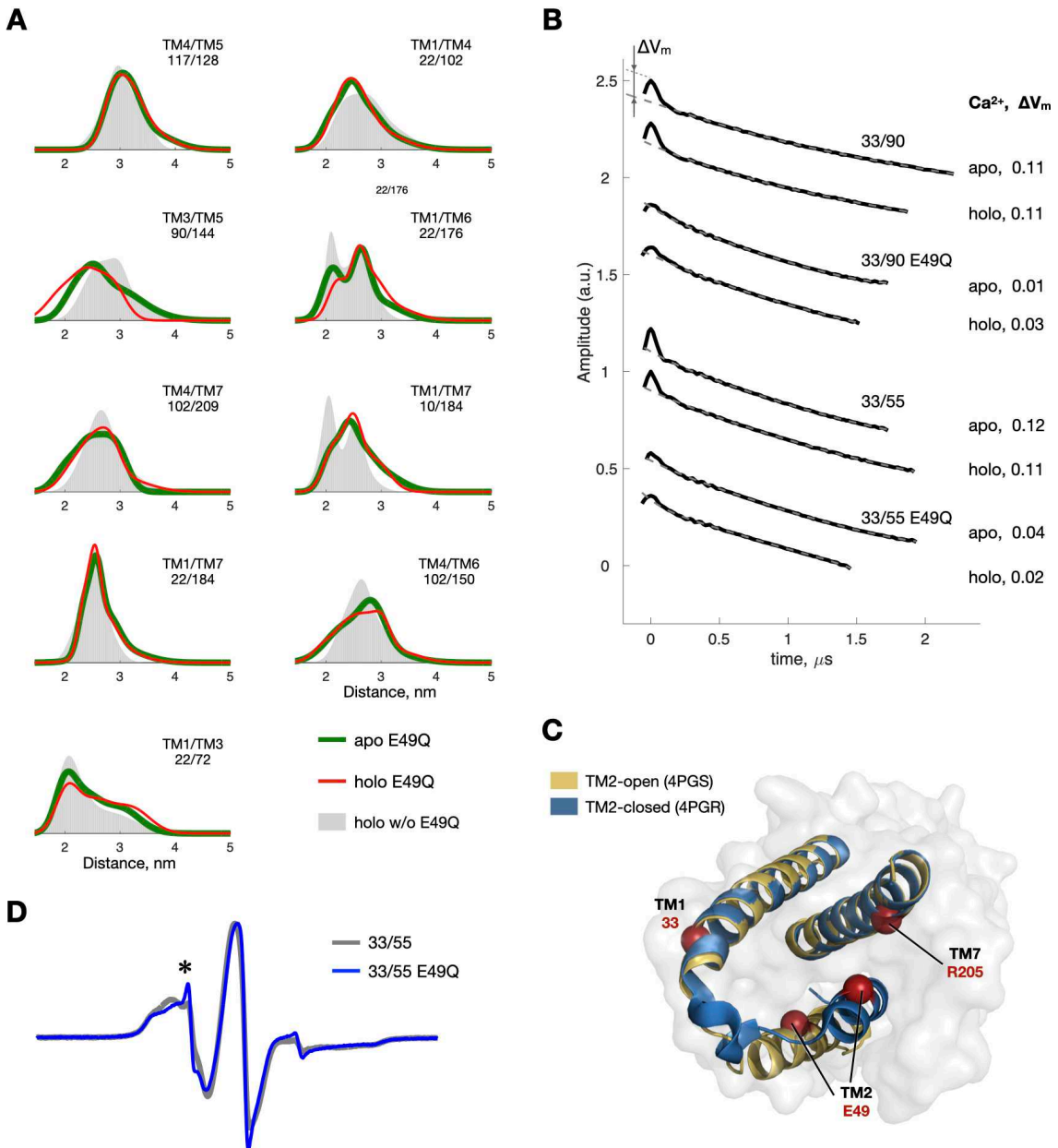


Fig. 3. Results of the DEER measurements for BsYetJ E49Q. (A) Distance distributions of BsYetJ E49Q variants in comparison with the holo BsYetJ without the E49Q mutation. (B) DEER traces of 33/90 and 33/55 to highlight the substantial changes in ΔV_m between BsYetJ with and without E49Q. (C) A cartoon illustration for the relative positions of 33 (TM1) and 49 (TM2). (D) CW-ESR spectra of 33/55 with and without E49Q. The spectrum of 33/55 R49Q displays a higher mobility (denoted by asterisk) than the other. The width of the magnetic field shown is 120 G.

Taken together with the result of Fluo-8 assay measurements (shown in Fig. 1), we proposed that the interactions (e.g., salt bridge or hydrogen bonds) between E49 and R205 are critical in stabilizing the TM2-closed conformation and are important in the regulation of calcium transport. The mutation E49Q disrupts the E49-R205 dyad, hence leading to the

disordering in the loop connecting TM1/TM2 and the large increase in $[Ca^{2+}]_{LUV}$ for BsYetJ E49Q.

MD simulations to confirm the DEER-derived structures

From the DEER-derived distances, we obtained two distinctly different structural models for BsYetJ in the ER nanodiscs, suggesting that the two structures exist in equilibrium in apo and holo states (Fig. 4A). Unbiased MD simulations were implemented to validate the derived structural models in the ER lipid bilayer, and root-mean-square deviation (RMSD) analysis was used to determine simulation convergence (Fig. S4A). There are two marked differences between the two DEER-derived structures (hereafter, referred to as DEER TM2-open and -closed). The first one lies in the conformation of TM2 showing a large lateral movement between the structures. The second one occurs in the helices from TM5 to TM7, which features relatively small differences between the two structures. The differences in TM1 and TM4 between the two DEER-derived structures are considered small and insignificant as they have the smallest RMSD values among the RMSD values of individual helices (Fig. S4B). In the MD simulations of DEER TM2-closed structure, a mean hydrogen bound number between E49 and R205 was found to be 1.25 over the simulation time from 30 to 500 ns (Fig. S4C), revealing the importance of the E49-R205 dyad in stabilizing the DEER TM2-closed structure. Our MD simulations show that water molecules can flow through the channel of the DEER TM2-open structure but are completely blocked in the DEER TM2-closed structure (Fig. S4D). Also, we simulated interspin distance distributions (Fig. S5) from the DEER-derived models using MtsslWizard program²². The simulations are reasonably consistent with the experimental DEER distance distributions, validating the two DEER-derived models.

Next, we explored the molecular details of the TM2-mediated channel using the channel annotation package (CHAP) that implements a methodology for predicting the conductive state of an ion channel structure with a consideration of pore dimensions and profile of pore hydrophobicity²³. The physical dimensions of the ion permeation pore were calculated from the DEER TM2-closed structure. The pore shown (Fig. 4B) is surrounded by TM2, TM5, TM6, and TM7. The narrowest cross-section (approximately, 4 Å in radius; Fig.

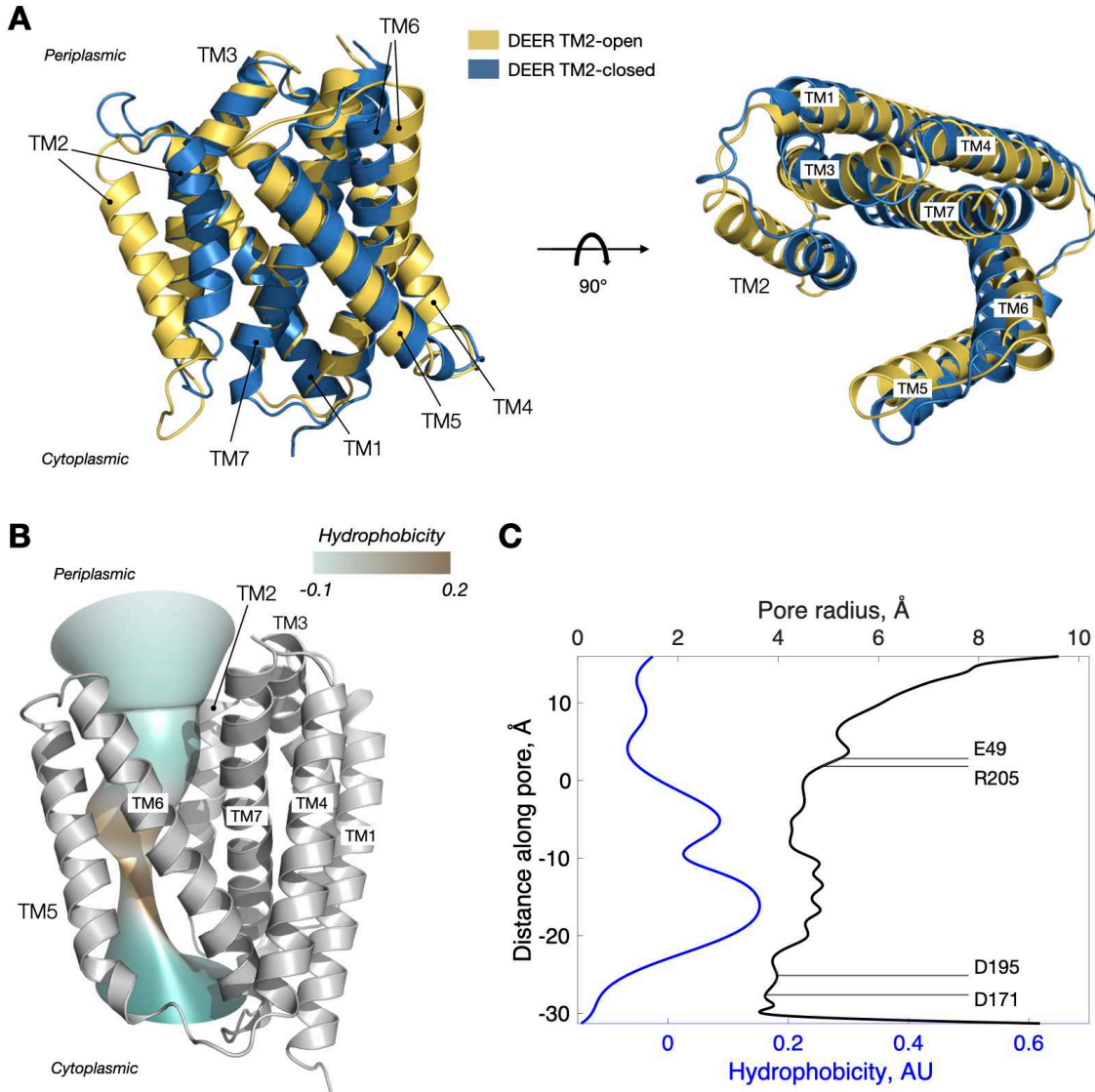


Fig. 4. DEER derived structural models of BsYetJ in the ER. (A) Structural models derived from the DEER results. (B) The TM2-mediated pore generated using the CHAP program, in the DEER TM2-closed model. (C) Dimensions and hydrophobicity profiles for the TM2-mediated pore.

4C) is located on the cytoplasmic side and bracketed by charged or large amino acids of TM6 and TM7 (Y170, D171, Q174, D195). Near the middle of the membrane-spanning pore, we observed a cluster of residues (A56, V133, V163, F164, L194) that causes a large increase in hydrophobicity and thus in energy barrier preventing ion and water leakage. In the cross area near to E49 and R205, the pore radius is approximately 5 Å and the degree of hydrophobicity is similar to that of the narrowest cross section (Fig. 4C). The distance between the side-chains of E49 and R205 in the DEER-derived structures varies, approximately, from 5 to 11

\AA , a range that may possibly coordinate with a calcium ion (diameter: 2.3 \AA , approximately) in a fully hydrated state^{24–27}. Altogether, our results support that the two terminal regions (D171/D195- and E49/R205-associated) as well as the hydrophobic region in the middle of the pore contribute to the inactivation of Ca^{2+} influx activity, suggesting there are more than one gating mechanism along the proposed TM2-mediated channel.

DISCUSSION

This study reveals new insights into the mechanism of Ca^{2+} transport activity of BsYetJ. We measured the Ca^{2+} influx activity of various BsYetJ variants carrying one or two mutations at the six highly conserved negatively charged residues (D121, E49, D171, E182, D183, and D195; Fig. 1A). We found that only when site E49 is mutated can we observe a large increase in $[\text{Ca}^{2+}]_{\text{LUV}}$ (3- or 4-fold greater than WT). This finding about E49 in the ER environment has not been reported and it is different from what was previously inferred from the detergent-solubilized crystal structures and the DEER-derived models in pure POPC environment. In the previous studies^{9–11}, D171 and D195 (also highly conserved residues; Fig. 1A) were proposed to play a key role in the Ca^{2+} transport activity. The present study shows that a single or double mutation in either or both two sites (D171 and D195) cause relatively small changes to the activity, as compared with the E49Q result. As the major difference in the experimental condition between the present and previous studies lies in the lipid environment, an important message received is that BsYetJ/TMBIM6 is a lipid-sensitive membrane protein. The difference in lipid environment leads to changes in structural conformations and thus the functional sites. Notably, It was shown that BsYetJ, though a bacterial TMBIM6 homolog, can mediate Ca^{2+} flux from ER Ca^{2+} stores (in a range from μM to low mM) in mammalian cells, suggesting that the Ca^{2+} flux activity of BsYetJ is conserved¹⁰. In that regard, our present results with the restoration of the ER environment are of high biological significance.

Our results also suggest that the highly conserved residue E49 works together with R205 in modulating the TM2-mediated Ca^{2+} influx activity, as a single point mutation in either of the two residues leads to a similar interference to the Ca^{2+} influx activity. Despite the large interference to the activity, BsYetJ E49Q (or E49A, R205A) does not completely lose the control on Ca^{2+} influx and retains a reduced ability to limit the influx of Ca^{2+} across

the membrane. For example, $[Ca^{2+}]_{LUV}$ of E49Q is, approximately, 300 nM (for 100 μM ∇Ca^{2+}) and 450 nM (for 500 μM ∇Ca^{2+}), both of which are lower than the concentration of entrapped Fluo-8 (10 μM) and the external Ca^{2+} concentrations. The greater the ∇Ca^{2+} is applied, the greater the $[Ca^{2+}]_{LUV}$ is obtained. Together with the pore analysis using the CHAP, our results suggest that in addition to the E49-associated one, there are other gating mechanisms at work. There are at least three putative gates regulating the calcium conductance of BsYetJ: two dyads of charged residues (i.e., E49-R205 and D171-D195) and one cluster of hydrophobic residues in the middle of the channel.

Taken together, we hypothesize a regulatory model for the observed calcium-dependent inactivation of BsYetJ at pH 7.4. BsYetJ adopts two major conformations in the ER environment. The charged residues E49 and R205 work closely to form the DEER TM2-closed conformation that blocks ion and water molecules from passing through the TM2-mediated channel. In the presence of Ca^{2+} , BsYetJ is constitutively in the DEER TM2-open form (as suggested from the DEER result 33/55) having Ca^{2+} bound in a hydrated form in the E49-R205 dyad and thus blocking any possible ion influx through the channel. However, the site is just one of possible Ca^{2+} binding sites along the channel. The E49-associated site has high binding affinity for Ca^{2+} and it would hold until a sufficiently high transmembrane gradient ∇Ca^{2+} is established, promoting a release of the chelated Ca^{2+} inward crossing the hydrophobic region to next binding sites. The affinity of the D171- or D195-associated site for Ca^{2+} is lower for sure as the mutations (shown in Fig. 1) in the D171-D195 dyad cause a relatively small change to the activity. The D171-D195 dyad is not as important as E49 site in the ER environment, as demonstrated in the present study. The D171-D195 dyad may act as a pH sensor or a gating site even in the ER, as previously reported in other lipid environments^{9,10}, warranting further investigations. To support that the D171-D195 dyad is less important than E49, we performed the Ca^{2+} influx activity of E49Q/D195N and found that it has a $[Ca^{2+}]_{LUV}$ much greater than E49Q (Fig. S6). Indeed, the D171-D195 dyad acts as a relatively minor selectivity filter than E49 in controlling the calcium influx activity. Although the coordination of Ca^{2+} at the proposed binding sites is not explicitly determined in the present study, the channel selectivity to Ca^{2+} is verified. Once the ∇Ca^{2+} declines to a lower level, the influx of Ca^{2+} across the membrane is limited and the TM2-mediated channel is inactivated.

We note that the force that counteracts further Ca^{2+} influx in a lower ∇Ca^{2+} level may include the increased electrical potential due to the accumulating Ca^{2+} in LUVs. Nevertheless, the gradient ∇Ca^{2+} definitely is the dominant force driving the Ca^{2+} influx at an early stage of the event. The observed inactivation of Ca^{2+} influx in BsYetJ depends on the Ca^{2+} gradient across membrane and the dependence is greater for BsYetJ E49Q than others, supporting a view that the E49-R205 dyad acts as a primary calcium-selectivity filter, an inactivation gate controlling the TM2-mediated influx of Ca^{2+} along the Ca^{2+} electrochemical gradient.

In summary, we used DEER and fluorescence techniques to follow conformational changes of BsYetJ associated with Ca^{2+} entry and accumulation in the ER lipid environment, unveiling the calcium dependent inactivation, a previously unanticipated function, in BsYetJ. The conformational changes are mainly confined to a distinct region associated with TM2, providing structure-based insights into how BsYetJ/TMBIM6 regulates its calcium transport activity by interconversion between distinct conformations.

MATERIALS AND METHODS

Expressions and purifications of BsYetJ

We followed the previously established protocol for expression and purification. A pET-24 derived pNYCOMP vector containing His-tag at C-terminus of BsYetJ was used^{9,11}. Plasmids encoding BsYetJ mutants were generated using a QuikChange mutagenesis kit at the indicated sites and verified by DNA sequencing. Briefly, the plasmid was transformed into *E. coli* pLysS BL21(DE3) (Agilent) by heat shock. For protein expression, 25 mL start-culture in Terrific Broth (TB) medium supplemented with 30 $\mu\text{g}/\text{mL}$ of kanamycin (Kan) and 25 $\mu\text{g}/\text{mL}$ of chloramphenicol (Cam) was grown at 37 °C with shaking overnight. A dense culture was used to inoculate 0.6 L of TB media supplemented with 30 $\mu\text{g}/\text{mL}$ of Kan and 25 $\mu\text{g}/\text{mL}$ of Cam. Cultures were grown at 37 °C with shaking to an OD600 above 1.0, and then protein was induced by the addition of 0.5 mM isopropyl 1-thio-β-D-galactopyranoside

(IPTG) at the same temperature for 4–6 h. The cells were harvested by centrifugation at 9000g for 5 min at 4 °C and stored at –80 °C until purification.

For protein purification, the frozen cell pellets were resuspended in 50 mL BsYetJ lysis buffer (50 mM HEPES, 0.3 M NaCl, 20 mM imidazole, 5% glycerol and 1 mM MgCl₂, pH 7.8) supplemented with 1 mM solution of phenylmethylsulfonyl fluoride (PMSF), 0.2 mg/mL lysozyme and a pinch of DNaseI, and then stirred for 1 h at room temperature. The resuspended pellet was sonicated by pulse sonication at 70% output on ice for 10 min, followed by centrifugation at 12800g for 30 min at 4 °C. Membrane pellets were obtained by the second centrifugation at 44300g for 1 h and then resuspended in the lysis buffer with an additional 1.5% (w/v) β-DDM. After being stirred at room temperature for 1 h, the supernatant containing solubilized membrane protein was cleaned up by centrifugation at 44300g for 10 min at 4 °C to remove insoluble components. The cleared lysate was filtrated through a 0.45 μm Nylon filter and loaded onto a 5 mL HisTrap HP column (GE Healthcare) pre-equilibrated with the BsYetJ lysis buffer supplemented with β-DDM to a final concentration of 0.05% (w/v). Unbound proteins were removed with 20 column volumes (CV) of BsYetJ wash buffer (50 mM HEPES, 0.5 M NaCl, 75 mM imidazole, 5% glycerol and 0.05% (w/v) β-DDM, pH 7.8) and bound BsYetJ was eluted with 6 CV of BsYetJ elution buffer (50 mM HEPES, 0.3 M NaCl, 0.5 M imidazole, 5% glycerol and 0.05% (w/v) β-DDM, pH 7.8). Eluted BsYetJ was buffer-exchanged into BsYetJ storage buffer (50 mM HEPES, 0.3 M NaCl, 2.5% (v/v) glycerol and 0.05% (w/v) β-DDM, pH 7.4) and concentrated to 4 mg/mL using a 50K MWCO concentrator (Amicon). Protein purity was checked by SDS-PAGE with Coomassie blue staining. The concentration of BsYetJ was determined using absorption spectroscopy at 280 nm (extinction coefficient 24410 M⁻¹ cm⁻¹).

As wild-type (WT) BsYetJ is a cysteine-free protein, its construct was directly used to prepare various cysteine variants of BsYetJ for spin-labeling study. Spin-labeling reaction was performed by addition of 40-fold molar excess of MTSSL (1-oxyl-2,2,5,5-tetramethylpyrroline-3-methyl methanethiosulfonate) (Enzo Life Sciences) from a 0.1 M stock solution in acetonitrile. The reaction was kept in dark overnight at 4 °C and then concentrated to ~10 mg/mL using Amicon Ultra-50K centrifugal filter units. Excess free spin labels were removed completely during the nanodisc preparation as described later.

His-tag free BsYetJ was used in this study. His-tag of BsYetJ was cleaved with the addition of a 1:15 molar ratio of TEV protease and gently tumbled at 4 °C overnight. The mixture was filtered through 0.22 µm PVDF filter and the cleaved protein was harvested by reverse purification on HisTrap HP column, collecting the flow through and wash fractions. Protein purity was checked by SDS-PAGE. Protein was concentrated to 4 mg/mL and stored in aliquots at –80 °C.

Expressions and purifications of membrane scaffold protein (MSP)

Membrane scaffold protein (MSP1D1, herein denoted by MSP for simplification) was expressed and purified as previously described^{28,29}. Briefly, MSP1D1 gene was cloned to pET-28a (Addgene) with a N-terminal His-tag. The plasmid was transformed into the *E. coli* BL21(DE3) expression strain (Agilent) by heat shock, plated on Luria-Bertani (LB)-agar plates supplemented with 30 µg/mL of Kan, and incubated at 37 °C overnight. A single colony was used to inoculate 25 mL start-culture in TB medium supplemented with 30 µg/mL of Kan at 37 °C with shaking overnight. The dense culture was used to inoculate a secondary culture in 0.6 L TB supplemented with 30 µg/mL of Kan. Cultures were grown at 37 °C with shaking to an OD600 above 1.0, and then protein was induced by the addition of 1 mM IPTG at 30 °C for 4–6 h. The cells were harvested by centrifugation at 9000g for 5 min at 4 °C and stored at –80 °C until purification. For protein purification, the frozen cell pellets were resuspended in 50 mL MSP lysis buffer (20 mM sodium phosphate, 0.1 M NaCl, 1% Triton X-100, 10 mM MgSO₄, pH 7.4) supplemented with 1 mM PMSF, 0.2 mg/mL lysozyme and a pinch of DNaseI, and then stirred for 1 h at room temperature. The resuspended pellet was sonicated by pulse sonication at 70% output on ice for 10 min, followed by centrifugation at 12800g for 50 min at 4 °C. The supernatant was filtrated through a 0.45 µm Nylon filter and loaded onto a 5 mL HisTrap HP column (GE Healthcare) pre-equilibrated with MSP lysis buffer. Unbound proteins were removed with the following order of buffer: (i) 5 CV of 40 mM Tris-HCl, 0.3 M NaCl, and 1% Triton X-100, pH 8.0 (ii) 5 CV of 40 mM Tris-HCl, 0.3 M NaCl, and 50 mM sodium cholate, pH 8.0 (iii) 5 CV of 40 mM Tris-HCl, 0.3 M NaCl, and 40 mM imidazole, pH 8.0. The bound MSP was eluted with 10 CV of MSP elution buffer (40 mM Tris-HCl, 0.3 M NaCl, and 0.4 M imidazole, pH 8.0), buffer-exchanged into MSP storage buffer (20 mM Tris-HCl and 0.1 M NaCl, pH 7.4) and

concentrated to 10 mg/mL using a 10K MWCO concentrator (Amicon). Protein purity was checked by SDS-PAGE with Coomassie blue staining. The concentration of MSP was determined using absorption spectroscopy at 280 nm (extinction coefficient 21430 M⁻¹ cm⁻¹).

Preparation of BsYetJ in lipid nanodiscs

Spin-labeled BsYetJ variants in β-DDM was reconstituted into MSP nanodiscs with a lipid composition of POPC:POPE:PI:cholesterol 61:20:11:8 (molar ratio) mimicking the ER^{30,31}, at a final molar ratio of 1:4:240 (BsYetJ: MSP: lipid mix). 1-palmitoyl-2-oleoyl-*sn*-glycero-3-phosphocholine (POPC), 1-palmitoyl-2-oleoyl-*sn*-glycero-3-phosphoethanolamine (POPE), and l- α -phosphatidylinositol (PI) were purchased from Avanti Polar Lipids. Briefly, 19.7 μ mole of the lipid mixture dissolved in chloroform was dried under a gentle stream of nitrogen gas for 30 min. The dried lipid was resuspended into a stored buffer supplemented with 200 μ L of 150 mM sodium cholate (SC), sonicated for 5 min, and then pipetted up and down until the lipid mixture became transparent. BsYetJ and MSP were added to the lipid mixture and mixed at room temperature for 5 min. This addition brought the final concentrations to approximately 44.6 μ M BsYetJ, 178.4 μ M MSP, 10.7 mM lipid mix, and 21.4 mM SC. To remove the detergent, the mix was then added into 1 mg/mL of biobeads SM-2 (Bio-Rad) and gently tumbled at 4 °C overnight. Biobeads were removed by a short spin-down and the nanodisc suspension was then run on a Superdex 200 Increase 10/300 GL gel filtration column (GE Healthcare) equilibrated with nanodisc buffer (50 mM HEPES and 0.1 M choline chloride, pH 7.4). Purified samples were concentrated with Amicon Ultra-50K centrifugal filter units.

BsYetJ reconstitution into liposomes

Reconstitution of BsYetJ into liposomes was performed as previously described with minor modifications¹¹. To avoid residual calcium, the extruder apparatus were washed with 1 mM EDTA and then assay buffer A (10 mM MOPS, pH 7.4, 20 mM NMDG, 300 μ M EGTA and 10 μ M Fluo-8) before starting the experiment. Briefly, 6.58 μ mole of lipid dissolved in chloroform was dried under a gentle stream of nitrogen gas for 30 min. The dried lipid was resuspended into 200 μ L of assay buffer A, followed by 5 min sonication. After 10 cycles of freeze-and-thaw, the suspension was extruded through a 400 nm filter (Whatman) 11 times.

Wash the filter four times with 200 μ L of assay buffer A and collect the wash to minimize the loss of lipid. The final volume of suspension was 1 mL. The resulting liposomes were destabilized by the addition of 20 μ L of 10% Triton X-100 and incubated for 30 min at room temperature. Purified BsYetJ was added into the liposomes in a lipid/protein molar ratio of 2000 and incubated for 2 h at 4 °C to allow spontaneous reconstitution of the proteins.

To remove detergent, the mix was added into 250 mg of pre-washed Bio-Beads SM-2 adsorbents (washed into assay buffer A without Fluo-8). This mix was incubated at 4 °C for 3 h before the addition of another 250 mg of Biobeads (for a total 500 mg of Biobeads per 1 mL of reaction). This final mixture was gently tumbled at 4 °C overnight. Bio-beads were removed by a short spin-down and the proteoliposomes were then harvested by centrifugation at 44300g for 2 h at 4 °C. The supernatant was discarded and the pellet was resuspended in 1 mL of assay buffer B (10 mM MOPS, pH 7.4, 20 mM NMDG, 5 μ M EGTA).

Fluorescence based assays for measuring the activity of calcium transport across membrane

Proteoliposomes of 100 μ L were added to the wells of a black polystyrene NCU 96-well plate (Thermo Scientific). Fluo-8 (AAT Bioquest; Fig. S1B) has been widely used as a calcium-sensitive probe^{32–34}. Fluorescence emission intensities of Fluo-8 (excitation at 488 nm, emission at 520 nm) F520 were recorded at 10 s intervals using a Synergy H1 Microplate Reader device (BioTek). After 5 min equilibrium at room temperatures, calcium influx activity is initiated by the addition of 0.1 mM or 0.5 mM CaCl₂ externally. When F520 reached to a steady state, the calcium ionophore, ionomycin (10 μ M), was then added to the proteoliposomes together with an additional 1 mM Ca²⁺. In the selectivity experiments, 50 mM LiCl or NaCl was first equilibrated with proteoliposomes for 5 min at room temperatures, followed by the addition of CaCl₂.

Calcium concentration within LUVs (referred to as [Ca²⁺]_{LUV}) was determined by $[Ca^{2+}]_{LUV} = K_d \times (F - F_{min}) / (F_{max} - F)$, where K_d (153 nM) is the equilibrium dissociation constant of Fluo-8 for Ca²⁺ at pH 7.4 calibrated using the Calcium calibration kit (FluoProbes). F is the intensity of F520. F_{min} is the F520 intensity measured before the external addition of calcium. F_{max} is the F520 intensity measured after the addition of

ionomycin to achieve a complete permeation of proteoliposomes. The data are presented as box-and-whisker plot showing the 25th and 75th percentiles along with the median. The upper and lower bars show the maximum and minimum values. All fluorescence experiments were repeated independently at least ten times, with at least three different batches of purified BsYetJ.

DEER measurement and analysis

For DEER measurements, BsYetJ nanodisc samples were buffer-exchanged into nanodisc buffer and prepared in the protein concentration range of 100–200 μM . Approximately, 35 μL solution volume was added into quartz ESR tube (i.d. 3 mm). All buffers in the DEER experiments were deuterated. In the holo condition, the concentration of calcium was 20 mM. A Bruker ELEXSYS E580-400 X-band CW/Pulsed spectrometer, with a split-ring resonator (EN4118X-MS3) and a helium gas flow system (4118CF and 4112HV), was used. The ESR probe head was precooled to 80 K prior to the transfer of the ESR sample tube into the cavity. DEER experiments were performed using the typical four-pulse constant-time DEER sequence^{12,35}. The detection pulses were set to 32 and 16 ns for π and $\pi/2$ pulses, respectively, and the pump frequency was set to approximately 65 MHz lower than the detection pulse frequency. The pulse amplitudes were chosen to optimize the refocused echo. The $\pi/2$ -pulse was employed with $+x/-x$ phase cycles to eliminate receiver offsets. The duration of the pumping pulse was about 32 ns, and its frequency was coupled into the microwave bridge by a commercially available setup (E580-400U) from Bruker. All pulses were amplified via a pulsed traveling wave tube (TWT) amplifier (E580-1030). The field was adjusted such that the pump pulse is applied to the maximum of the nitroxide spectrum, where it selects the central $m_l = 0$ transition of A_{zz} together with the $m_l = \pm 1$ transitions. The accumulation time for each set of data was about 10 h at a temperature of 80 K. A common cooling approach was used. The sample tube was plunge-cooled in liquid nitrogen and then transferred into the ESR probehead, which was precooled to 80 K using a helium flow system.

Determination of interspin distance distribution of the DEER spectroscopy was performed using home-written program operating in the Matlab (MathWorks) as previously described and demonstrated^{11,14,36}. Basically, the data were analyzed using the Tikhonov regularization based on the L-curve method, followed by a data refinement process using the

maximum entropy method (MEM) to obtain the non-negative distance distributions^{20,21,37,38}. Error propagation in Tikhonov regularization cannot be predicted analytically. As demonstrated in the DeerAnalysis program, a common approach is to vary the starting time for the background fit and also add 50% noise of the original noise level to estimate uncertainty in the distance distributions. This study took the same method to obtain the uncertainty. To further validate the MEM-obtained distance distributions, we also analyzed DEER data using the approach combining the two program tools, DeerAnalysis and DEERconstruct^{21,39}. The major peaks of the distance distributions obtained from the MEM and the DeerAnalysis approaches are consistent with each other.

Derivation of the structural models from DEER distance distributions

The DEER TM2-closed and -open models were derived from the crystal TM2-closed (4PGR) and TM2-open (4PGS) structures, respectively. Seven TM helices were considered rigid bodies during structural rearrangements and linked by flexible peptide regions. Rigid-body rearrangements were generated by changing sidechain χ_1 and χ_2 dihedral angles in all regions, and backbone ϕ , ψ dihedral angles in the flexible regions randomly. After rejecting rearrangements with clashes ($< 2.5 \text{ \AA}$), the MtsslWizard program was used to simulate distance distributions of over 200000 rearrangements. The rearrangements with the smallest difference between MtsslWizard-predicted distance distribution and DEER distance distribution (Fig. 4A) were subjected to MD simulation to verify the structural models in the ER membrane and used in the CHAP analysis.

MD simulation and analysis

ER lipid bilayers containing 344 to 347 POPC, 119 to 120 POPE, 60 to 61 POPI, and 40 to 42 cholesterols were generated with CHARMM-GUI⁴⁰. The DEER-derived models of BsYetJ were placed in the ER membrane using PSFGEN utility of Visual Molecular Dynamics (VMD)^{41,42}. Systems were soaked in TIP3P water boxes and neutralized by adding Na^+ and Cl^- at the experimental condition (100 mM) using VMD's solvate and autoionize modules. The dimensions of the box were $150 \text{ nm} \times 150 \text{ nm} \times 110 \text{ nm}$. Simulations were performed using nanoscale molecular dynamics (NAMD) with CHARMM36 force field for proteins and lipids⁴³⁻⁴⁵. Simulations were carried out using periodic boundary conditions in the NPT

ensemble, particle mesh Ewald method, SHAKE algorithm, a non-bonded cutoff of 1.2 nm, and a 2 fs time step^{46–48}. Systems were kept at 300 K and 1 bar using Langevin dynamics. We performed energy minimization (100000 steps) of each structural model to remove bad contacts. After the equilibrium for 2 ns in the presence of harmonic constraints acting on the protein for membrane relaxation, production runs were performed for 200 ns. Coordinates, velocities, energies, and pressures were recorded for analysis every 1 ps. The root-mean-square deviation (RMSD) in comparison with the initial structures was calculated considering C α atoms using VMD’s RMSD trajectory tool.

Analysis of the sequence conservation

Analysis of sequence conservation of the selected amino acids in BsYetJ and the multiple sequence alignment were performed using ConSurf web server and WebLogo, as detailed in the supplementary figure (Fig. S1)^{49–51}.

ACKNOWLEDGEMENTS

This work was supported by grants (108-2113-M-007-029 and 111-2731-M-007-001) from the Ministry of Science and Technology of Taiwan and the Frontier Research Center on Fundamental and Applied Sciences of Matters at NTHU. All the ESR measurements were conducted in the Research Instrument Center of Taiwan located at NTHU. YJL, CCL, TYK, and YWC conceived the experiments. YJL, CCC, SCC, and HYC performed biochemical experiments. TYK conducted MD simulations. YJL, CCL, TYK, and YWC analyzed the data. YJL, CCC, SCC, and HYC conducted ESR/DEER experiments. YWC supervised the work. YJL, CCC, TYK, and YWC wrote the manuscript. All authors edited the manuscript. The authors declare that they have no competing interests. All data needed to evaluate the conclusions in the paper are present in the paper and/or the Supplementary Materials.

REFERENCES

1. Rojas-Rivera, D. & Hetz, C. TMBIM protein family: ancestral regulators of cell death. *Oncogene* **34**, 269–280 (2015).
2. Carrara, G., Saraiva, N., Gubser, C., Johnson, B. F. & Smith, G. L. Six-transmembrane Topology for Golgi Anti-apoptotic Protein (GAAP) and Bax Inhibitor 1 (BI-1) Provides Model for the Transmembrane Bax Inhibitor-containing Motif (TMBIM) Family. *Journal of Biological Chemistry* **287**, 15896–15905 (2012).
3. Liu, Q. TMBIM-mediated Ca(2+) homeostasis and cell death. *Biochimica et biophysica acta* **1864**, 850–857 (2017).
4. Lisak, D. A. *et al.* The transmembrane Bax inhibitor motif (TMBIM) containing protein family: Tissue expression, intracellular localization and effects on the ER CA2+-filling state. *Biochimica et Biophysica Acta - Molecular Cell Research* **1853**, 2104–2114 (2014).
5. Henke, N. *et al.* The ancient cell death suppressor BAX inhibitor-1. *Cell Calcium* **50**, 251–260 (2011).
6. Pihán, P. *et al.* Control of lysosomal-mediated cell death by the pH-dependent calcium channel RECS1. *Sci. Adv.* **7**, eabe5469 (2021).
7. Kim, H.-K. *et al.* TMBIM6/BI-1 contributes to cancer progression through assembly with mTORC2 and AKT activation. *Nat Commun* **11**, 4012 (2020).
8. Carrara, G. *et al.* Golgi Anti-apoptotic Proteins Are Highly Conserved Ion Channels That Affect Apoptosis and Cell Migration. *Journal of Biological Chemistry* **290**, 11785–11801 (2015).
9. Chang, Y. *et al.* Structural basis for a pH-sensitive calcium leak across membranes. *Science* **344**, 1131–1135 (2014).
10. Guo, G. *et al.* Ion and pH Sensitivity of a TMBIM Ca2+ Channel. *Structure* **27**, 1013-1021.e3 (2019).

11. Li, C.-C., Kao, T.-Y., Cheng, C.-C. & Chiang, Y.-W. Structure and regulation of the BsYetJ calcium channel in lipid nanodiscs. *Proc Natl Acad Sci USA* **117**, 30126–30134 (2020).
12. Jeschke, G. DEER Distance Measurements on Proteins. *Annu. Rev. Phys. Chem.* **63**, 419–446 (2012).
13. Schiemann, O. *et al.* Benchmark Test and Guidelines for DEER/PELDOR Experiments on Nitroxide-Labeled Biomolecules. *J. Am. Chem. Soc.* **143**, 17875–17890 (2021).
14. Tsai, R.-F. *et al.* Nitrosylation of the Diiron Core Mediated by the N Domain of YtfE. *J. Phys. Chem. Lett.* **11**, 8538–8542 (2020).
15. daCosta, C. J. B. & Baenziger, J. E. A Lipid-dependent Uncoupled Conformation of the Acetylcholine Receptor. *Journal of Biological Chemistry* **284**, 17819–17825 (2009).
16. Cheng, W. W. L., D’Avanzo, N., Doyle, D. A. & Nichols, C. G. Dual-Mode Phospholipid Regulation of Human Inward Rectifying Potassium Channels. *Biophysical Journal* **100**, 620–628 (2011).
17. Carswell, C. L., Sun, J. & Baenziger, J. E. Intramembrane Aromatic Interactions Influence the Lipid Sensitivities of Pentameric Ligand-gated Ion Channels. *Journal of Biological Chemistry* **290**, 2496–2507 (2015).
18. Kumar, P. *et al.* Cryo-EM structures of a lipid-sensitive pentameric ligand-gated ion channel embedded in a phosphatidylcholine-only bilayer. *Proc. Natl. Acad. Sci. U.S.A.* **117**, 1788–1798 (2020).
19. Luganini, A. *et al.* Human cytomegalovirus US21 protein is a viroporin that modulates calcium homeostasis and protects cells against apoptosis. *Proc. Natl. Acad. Sci. U.S.A.* **115**, (2018).

20. Chiang, Y.-W., Borbat, P. P. & Freed, J. H. The determination of pair distance distributions by pulsed ESR using Tikhonov regularization. *J. Magn. Reson.* **172**, 279–295 (2005).
21. Jeschke, G. *et al.* DeerAnalysis2006—a comprehensive software package for analyzing pulsed ELDOR data. *Appl. Magn. Reson.* **30**, 473–498 (2006).
22. Hagelueken, G., Abdullin, D. & Schiemann, O. mtsslSuite: Probing Biomolecular Conformation by Spin-Labeling Studies. in *Methods in Enzymology* 595–622 (2015). doi:10.1016/bs.mie.2015.06.006.
23. Klesse, G., Rao, S., Sansom, M. S. P. & Tucker, S. J. CHAP: A Versatile Tool for the Structural and Functional Annotation of Ion Channel Pores. *Journal of Molecular Biology* **431**, 3353–3365 (2019).
24. Bavi, N. *et al.* The conformational cycle of prestin underlies outer-hair cell electromotility. *Nature* **600**, 553–558 (2021).
25. Zhorov, B. S. Possible Mechanism of Ion Selectivity in Eukaryotic Voltage-Gated Sodium Channels. *J. Phys. Chem. B* **125**, 2074–2088 (2021).
26. Jalilehvand, F. *et al.* Hydration of the Calcium Ion. An EXAFS, Large-Angle X-ray Scattering, and Molecular Dynamics Simulation Study. *J. Am. Chem. Soc.* **123**, 431–441 (2001).
27. Delgado, A. A. A., Sethio, D., Munar, I., Aviyente, V. & Kraka, E. Local vibrational mode analysis of ion–solvent and solvent–solvent interactions for hydrated Ca²⁺ clusters. *J. Chem. Phys.* **153**, 224303 (2020).
28. Martens, C. *et al.* Lipids modulate the conformational dynamics of a secondary multidrug transporter. *Nature Structural & Molecular Biology* **23**, 744–751 (2016).

29. Li, C.-C., Hung, C.-L., Yeh, P.-S., Li, C.-E. & Chiang, Y.-W. Doubly spin-labeled nanodiscs to improve structural determination of membrane proteins by ESR. *RSC Adv.* **9**, 9014–9021 (2019).
30. Casares, D., Escribá, P. V. & Rosselló, C. A. Membrane Lipid Composition: Effect on Membrane and Organelle Structure, Function and Compartmentalization and Therapeutic Avenues. *IJMS* **20**, 2167 (2019).
31. Escribá, P. V. *et al.* Membrane lipid therapy: Modulation of the cell membrane composition and structure as a molecular base for drug discovery and new disease treatment. *Progress in Lipid Research* **59**, 38–53 (2015).
32. Muller, M. S. & Taylor, C. W. ATP evokes Ca^{2+} signals in cultured foetal human cortical astrocytes entirely through G protein-coupled P2Y receptors. *J. Neurochem.* **142**, 876–885 (2017).
33. Schober, J. *et al.* NNC 26-9100 increases $\text{A}\beta 1\text{-}42$ phagocytosis, inhibits nitric oxide production and decreases calcium in BV2 microglia cells. *PLoS ONE* **16**, e0254242 (2021).
34. Peters, C. J. *et al.* The Sixth Transmembrane Segment Is a Major Gating Component of the TMEM16A Calcium-Activated Chloride Channel. *Neuron* **97**, 1063-1077.e4 (2018).
35. Pannier, M., Veit, S., Godt, A., Jeschke, G. & Spiess, H. W. Dead-Time Free Measurement of Dipole-Dipole Interactions between Electron Spins. *J Magn Reson* **142**, 331–340 (2000).
36. Lan, Y.-J. *et al.* Anti-apoptotic BCL-2 regulation by changes in dynamics of its long unstructured loop. *Commun. Biol.* **3**, 668 (2020).

37. Chiang, Y.-W., Borbat, P. P. & Freed, J. H. Maximum entropy: A complement to Tikhonov regularization for determination of pair distance distributions by pulsed ESR. *J. Magn. Reson.* **177**, 184–196 (2005).
38. Jeschke, G., Panek, G., Godt, A., Bender, A. & Paulsen, H. Data analysis procedures for pulse ELDOR measurements of broad distance distributions. *Applied Magnetic Resonance* **26**, 223–244 (2004).
39. Casey, T. M. & Fanucci, G. E. Spin labeling and Double Electron-Electron Resonance (DEER) to Deconstruct Conformational Ensembles of HIV Protease. in *Methods in Enzymology* 153–187 (2015). doi:10.1016/bs.mie.2015.07.019.
40. Jo, S., Kim, T., Iyer, V. G. & Im, W. CHARMM-GUI: A web-based graphical user interface for CHARMM. *J. Comput. Chem.* **29**, 1859–1865 (2008).
41. Jorgensen, W. L., Chandrasekhar, J., Madura, J. D., Impey, R. W. & Klein, M. L. Comparison of simple potential functions for simulating liquid water. *The Journal of Chemical Physics* **79**, 926–935 (1983).
42. Humphrey, W., Dalke, A. & Schulten, K. VMD: Visual molecular dynamics. *Journal of Molecular Graphics* **14**, 33–38 (1996).
43. Phillips, J. C. *et al.* Scalable molecular dynamics with NAMD. *Journal of Computational Chemistry* **26**, 1781–1802 (2005).
44. Best, R. B. *et al.* Optimization of the Additive CHARMM All-Atom Protein Force Field Targeting Improved Sampling of the Backbone ϕ , ψ and Side-Chain χ_1 and χ_2 Dihedral Angles. *J. Chem. Theory Comput.* **8**, 3257–3273 (2012).
45. Klauda, J. B. *et al.* Update of the CHARMM All-Atom Additive Force Field for Lipids: Validation on Six Lipid Types. *J. Phys. Chem. B* **114**, 7830–7843 (2010).

46. Weber, W., Hünenberger, P. H. & McCammon, J. A. Molecular Dynamics Simulations of a Polyalanine Octapeptide under Ewald Boundary Conditions: Influence of Artificial Periodicity on Peptide Conformation. *The Journal of Physical Chemistry B* **104**, 3668–3675 (2000).
47. van Gunsteren, W. F. & Berendsen, H. J. C. Algorithms for macromolecular dynamics and constraint dynamics. *Molecular Physics* **34**, 1311–1327 (1977).
48. Darden, T., York, D. & Pedersen, L. Particle mesh Ewald: An $N \cdot \log(N)$ method for Ewald sums in large systems. *The Journal of Chemical Physics* **98**, 10089–10092 (1993).
49. Ashkenazy, H., Erez, E., Martz, E., Pupko, T. & Ben-Tal, N. ConSurf 2010: calculating evolutionary conservation in sequence and structure of proteins and nucleic acids. *Nucleic Acids Research* **38**, W529–W533 (2010).
50. Ashkenazy, H. *et al.* ConSurf 2016: an improved methodology to estimate and visualize evolutionary conservation in macromolecules. *Nucleic Acids Res* **44**, W344–W350 (2016).
51. Crooks, G. E., Hon, G., Chandonia, J.-M. & Brenner, S. E. WebLogo: A Sequence Logo Generator: Figure 1. *Genome Res.* **14**, 1188–1190 (2004).

Supplementary Files

This is a list of supplementary files associated with this preprint. Click to download.

- [SI.pdf](#)